ADVANCED FUNCTIONAL MATERIALS
www.afm-journal.de

Check for updates

Electrochemical Control of Charge Current Flow in Nanoporous Graphene

Isaac Alcón, Gaetano Calogero, Nick Papior,* and Mads Brandbyge*

During the last decade, on-surface fabricated graphene nanoribbons (GNRs) have gathered enormous attention due to their semiconducting π-conjugated nature and atomically precise structure. A significant breakthrough is the recent fabrication of nanoporous graphene (NPG) as a 2D array of laterally bonded GNRs. This covalent integration of GNRs could enable complex electronic functionality at the nanoscale; however, for that, it is crucial to externally control the electronic coupling between GNRs within NPGs, which, to date, has not been possible. Using quantum chemical calculations and large-scale transport simulations, this study demonstrates that such control is enabled in a newly designed quinone-NPG (q-NPG) thanks to its GNRs inter-connections based on electroactive para-benzoquinone units. As a result, the spatial distribution of injected currents in q-NPG may be tuned, with sub-nanometer precision, via the application of external electrostatic gates and electrochemical means. These results thus provide a fundamental strategy to design organic nanodevices with built-in externally tunable electronics and spintronics, which is key for future applications such as bio-chemical nanosensing and carbon nanoelectronics.

1. Introduction

During the last 15 years a new methodology for the fabrication of carbon nanostructures has emerged: that of bottom-up on-surface synthesis.[1,2] Specifically designed organic molecules are deposited on metallic substrates where they self-assemble and, by increasing temperature, they bind through a surface-catalyzed reaction via specific functional groups, forming highly robust covalent nanostructures.[3] Over the years, a number of different types of carbon nanomaterials have been fabricated in this way, such as extended 2D covalent organic frameworks,[2,4,5] 1D and circular molecular oligomers,[3,6–8] 1D organic polymers,[9–11] and nanographenes.[12–15] Among all these, the so-called graphene nanoribbons[16,17] (GNRs), first reported via on-surface synthesis in 2010,[18] have received enormous attention as potential platforms for future carbon nanoelectronics.[19–22] This is partly because of their fully π-conjugated structure allowing for efficient electron transport, plus their confined dimensionality equipping them with an electronic band gap which is essential for logic-gate applications. In this direction, electron transport through GNRs has been measured multiple times in solid-state devices[23–26] and also on metallic surfaces using the tip of a scanning tunneling microscope (STM).[27,28]

The covalent integration of GNRs into more complex carbon nanostructures represents a potential means to realize additional functionality at the nanoscale,[29] such as in the form of GNR-GNR[30–33] and GNR-molecular[34] heterojunctions. In this direction, a major step was the fabrication of the so-called nanoporous graphene (NPG) as a covalent array of laterally bonded GNRs.[35] NPG, which was tested in solid-state devices, could be regarded as the first instance of a full-carbon nanocircuit composed of parallel nanoelectronic channels (GNRs).[35] Importantly, it has been shown that other types of NPGs may be fabricated by lateral fusion of more complex chevron-type GNRs,[36] which demonstrates the generality of this approach. However, towards the applicability of NPGs for carbon nanoelectronics it is necessary that the electronic coupling between the GNRs within the 2D materials may be controlled, because that in turn would allow externally tuning the spreading or confinement of injected currents.[37]

In the fabricated NPG, GNRs are electronically coupled due to direct C-C π-conjugated bonds between neighboring channels.[35,37] It has been recently shown that GNRs may be laterally connected through benzene rings[38] which, in turn, due to destructive quantum interference (QI),[39,40] electronically decouples GNRs within NPGs.[41] However, for real-world

Dr. I. Alcón
Institut für Chemie und Biochemie
Physikalische und Theoretische Chemie
Freie Universität Berlin
Arnimallee 22, 14195 Berlin, Germany
E-mail: ialcon@zedat.fu-berlin.de
Dr. G. Calogero
CNR Institute for Microelectronics and Microsystems (CNR-IMM)
Strada VIII, 5, Catania 95121, Italy
Dr. N. Papior
Computing Center
Technical University of Denmark
Kongens Lyngby DK-2800, Denmark
E-mail: nicpa@dtu.dk
Prof. M. Brandbyge
Department of Physics
Technical University of Denmark and Center for Nanostructured Graphene (CNG)
Kongens Lyngby DK-2800, Denmark
The ORCID identification number(s) for the author(s) of this article can be found under https://doi.org/10.1002/adfm.202104031.

© 2021 The Authors. Advanced Functional Materials published by Wiley-VCH GmbH. This is an open access article under the terms of the Creative Commons Attribution License, which permits use, distribution and reproduction in any medium, provided the original work is properly cited.

DOI: 10.1002/adfm.202104031

© 2021 The Authors. Advanced Functional Materials published by Wiley-VCH GmbH

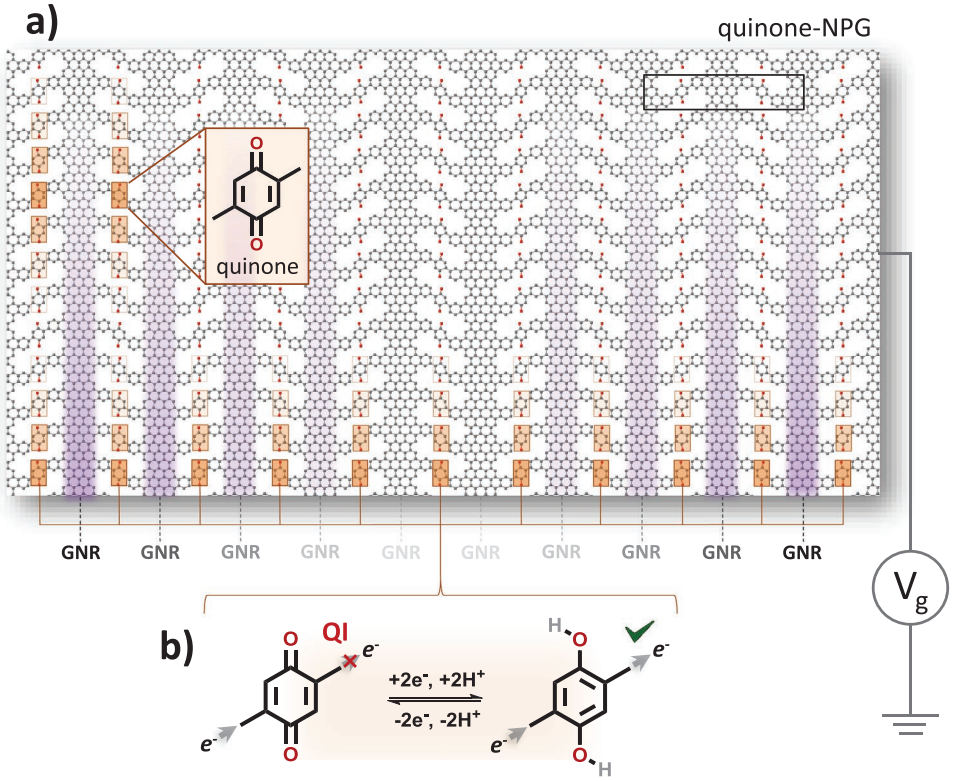

Figure 1. a) New type of NPGs proposed in this work, where GNRs are covalently connected via electroactive quinone units (orange boxes) providing an electrochemical control (e.g., via electrostatic gates, Vg) of the inter-channel electronic coupling. At the top right corner we depict the periodic unit cell utilized in this work to model NPGs. b) Upon electrochemical reduction via hydrogen passivation the quinoidal configuration is converted into an aromatic configuration, which deactivates QI within the ring, increasing electron conductivity.[43]

applications such as biochemical sensing or logic-circuitry it would be highly desirable to manipulate such electronic coupling via external means (e.g., electrostatic gates). In this work we propose a promising strategy based on the usage of electroactive compounds, such as quinones, as organic bridges between GNRs in newly designed NPGs (**Figure 1**a). QI occurs in a number of quinoidal derivatives with different chemical structures.[42] However, more importantly, it has been shown that QI may be externally switched off in quinone-based single-molecule break junctions by electrochemical reduction, restoring electron transport through the molecular device.[43] This effect may be understood by the transformation along the redox process from the quinoidal electronic configuration into an aromatic one (see Figure 1b). Therefore, using electroactive quinone units as bridges between GNR channels could be the basis for a new class of NPGs with electrochemically tunable transport characteristics. Recent studies have shown that the edge of GNRs can be functionalized with quinone derivatives,[44] which further supports the experimental viability of this approach.

Here we assess, via first principles density functional theory (DFT) calculations and large-scale transport simulations, the potential of newly designed NPGs with quinone bridges as electroactive nanodevices. We find that such quinoidal NPGs show an electron/hole asymmetry in their neutral state, pointing to distinct transport characteristics for different doping. In order to explore that we apply different electrostatic gates doping the system with holes or electrons, respectively. We study the electronic changes of the material for each situation, and simulate the injection of currents in the associated large-scale gated devices. Our results demonstrate that as long as the quinoidal units remain in their neutral state, such as for positive gating, GNRs are electronically decoupled due to QI. Contrary, negative gating dopes the quinoidal bridges with electrons, restoring GNRs electronic coupling. Interestingly, such electron doping occurs only in one spin channel, which gives rise to very appealing spin-filtering effects on injected currents. Finally, inspired by single-molecule break junction experiments,[43] we test hydrogenation as an alternative tool to tune electronic coupling in a permanent (gate independent) local fashion. This allows us to propose a top-down post-treatment approach to realize complex nanoelectronic functionality with sub-nanometer precision.

2. Results

2.1. Materials Design and Characterization

In this work we propose the quinone-NPG (q-NPG), where GNRs are connected with para-benzoquinone units (top panel in **Figure 2**a), as a platform for electrochemically controlled charge transport. The atomic and electronic structure of q-NPG has been fully optimized using periodic DFT calculations and

© 2021 The Authors. Advanced Functional Materials published by Wiley-VCH GmbH

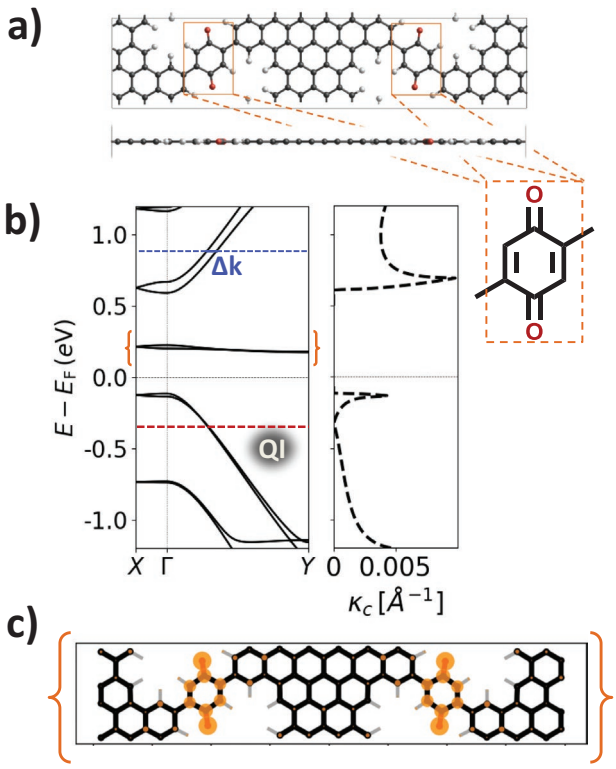

Figure 2. a) Periodic atomistic models for q-NPG, with a sketch of the chemical structure of quinone bridges (orange box). b) Associated electronic band structure (left panel) and κ_c spectra (right panel), the latter obtained from the electronic momentum difference as $\kappa_c = \Delta k/4$ at a given energy (see horizontal blue dashed line). The QI energy is indicated with a horizontal red dashed line. c) Local density of states at $E - E_F = 0.2$eV (orange) where the quinoidal crystal orbitals are energetically located.

the PBE functional[45] (see Methods for details). Other DFT flavors, such as the HSE06 hybrid functional,[46] give rise to qualitatively similar results (see Figure S1, Supporting Information). As outlined in Figure 2a, the two peripheral oxygen atoms per bridge generate the quinoidal electronic configuration. We note the bridging aryl rings may be slightly rotated out of plane, but such conformational changes have a negligible effect on the resulting electronic structure (see Figure S1, Supporting Information). Therefore we focus on the fully flat conformation, which will greatly facilitate the simulation of quantum transport in large-scale devices (see below).

As previously proposed, the inter-channel coupling coefficient (κ_c) can be used as an effective measure of how electronically coupled GNRs are in NPGs.[37] The κ_c may be extracted from the band structure of the 2D material as the momentum difference of the longitudinal bands (i.e., those with high dispersion along the GNRs direction) at a specific energy point ($\kappa_c = \Delta k/4$).[37] Moderately high κ_c values are thus associated to strongly electronically coupled GNRs, whereas low κ_c values are indicative of an electronically decoupled GNR array.[41]

Figure 2b shows the electronic band structure of q-NPG and the resulting κ_c spectra as calculated from the momentum difference (see Δk in Figure 2b). As we may see, QI takes place only in the valence band around $E - E_F = -0.3$eV (see red dashed line), but not in the conduction band. Interestingly, as shown in the right hand-side panel in Figure 2b, this causes an electron/hole asymmetry for κ_c which suggests that the spreading/confinement of electronic currents in this material could be controlled by external electrostatic gates. Besides the electron–hole asymmetry we also note the appearance of nearly flat unoccupied bands right above the Fermi energy (E_F; see orange brackets in the band structure in Figure 2b). The associated local density of states at $E - E_F = 0.2$eV (Figure 2c) shows that such bands correspond to the quinoidal electronic system fully localized in the para-benzoquinoidal bridges. The energetic position of the quinoidal band depends on the nature of the peripheral functional groups generating quinonization (see Figure S2, Supporting Information) and oxygen appears to be sufficiently electronegative to push down such unoccupied quinoidal bands right within the band gap. Such energetic stabilization of the quinoidal electronic system is responsible for the electron–hole asymmetry in the κ_c spectrum (right panel in Figure 2b) which is lifted, for instance, when the peripheral oxygen atoms are replaced by methyl groups (see Figure S2, Supporting Information).

2.2. p-type Gating – Spreading versus Confinement

In order to assess more in detail the electronic tunability of q-NPG for solid-state devices we modelled the effect of electrostatic gates by including in our periodic simulations a plane of charge (gate) placed 15Å below the 2D material (see Section 4 for details). As a starting point, we utilized a negatively charged gate inducing the counter charge (i.e., hole injection) in q-NPG, as schematically represented in **Figure 3**a. As we may see in Figure 3b, upon removing 7.1×10^{12} e cm^{-2}, the valence band associated with the GNR channels are de-populated (see local density of states at the E_F for this gate in Figure 3d). Such doping is not enough to place the E_F at the QI point, where κ_c is minimal (see right-hand side plot in Figure 3b), and so we need to extract 2.0×10^{13} e cm^{-2} from the 2D material in order to reach the QI point where $\kappa_c \approx 0$ (see Figure 3c).

In order to discern the effect of such gate application on the spreading of injected currents we constructed large-scale gated devices (80×120 nm^2) made of q-NPG, based on an efficient DFT-parameterized tight-binding (TB) model which enables transport simulations at such sizes (see Section 4, and Figure S3, Supporting Information). The q-NPG samples were constructed by repeating the periodic unit cell 20× along the *x*-direction and 140× along the y-direction, as schematically represented in Figure 3d, giving rise to a NPG sample containing 268 800 atoms. Figure 3e,f show bond-current maps upon injecting electrons at the central/lower part of the devices (see red dot) at each considered gate. We may see that upon extracting 7.1×10^{12} e cm^{-2}, which places the E_F at the onset of the valence band (see associated κ_c peak in Figure 3b), injected currents spread through a number of GNRs forming the so-called Talbot interference pattern.[37,41] Contrary, upon removing 2.0×10^{13} e cm^{-2}, the E_F hits the QI point and, as shown in Figure 3f, injected currents remain fully confined in the single central GNR where they were injected for distances longer than 100 nm from the source. Such behavior arises from the lack

© 2021 The Authors. Advanced Functional Materials published by Wiley-VCH GmbH

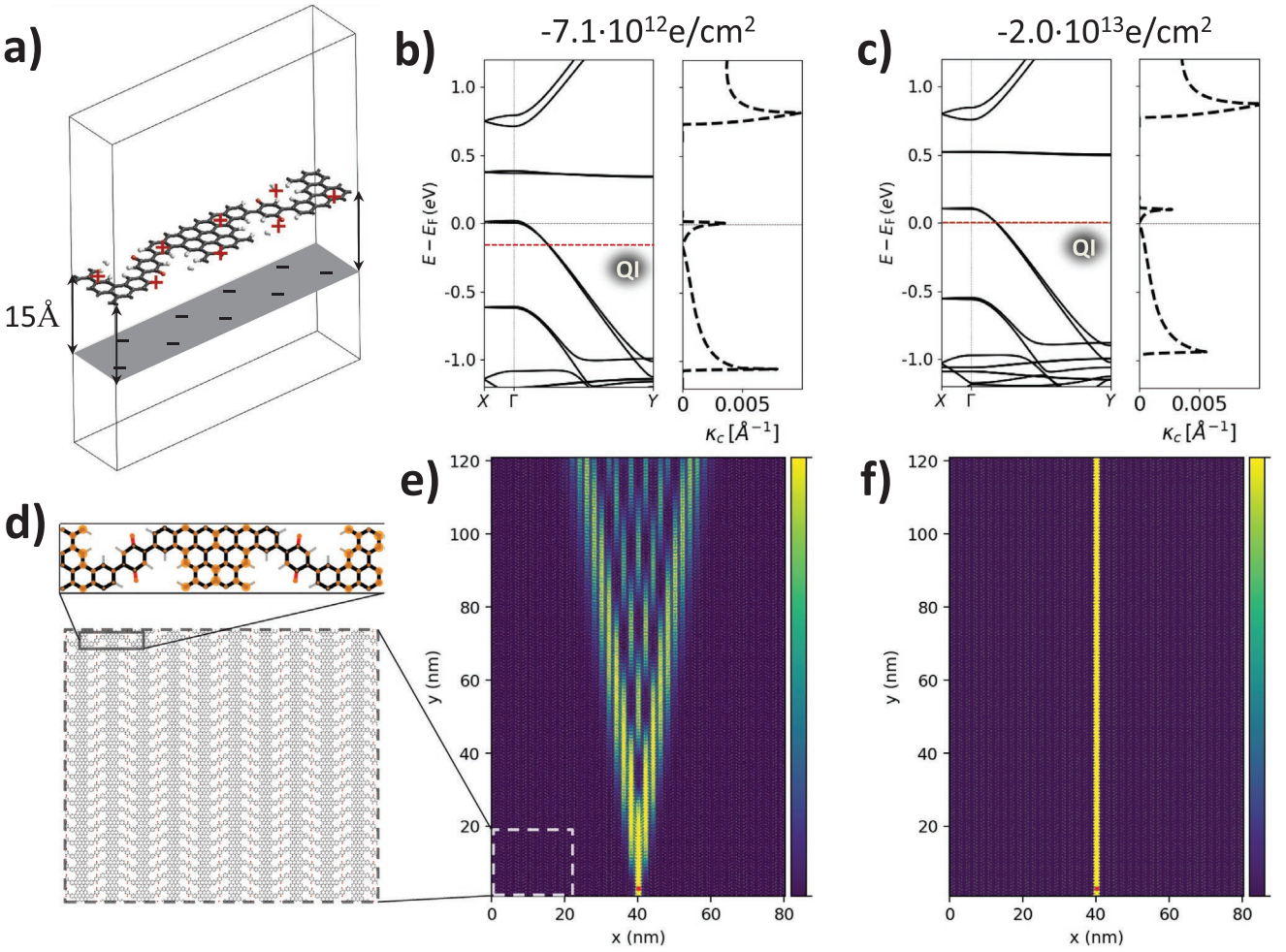

Figure 3. a) p-gating outline: A plane of negative charge at 15Å from the q-NPG induces a counter positive charge in the 2D material. Band structures (left) and associated κ_c (= $\Delta k/4$) spectra (right) upon gating b) -7.1×10^{12} e cm^{-2} and c) -2.0×10^{13} e cm^{-2} (–0.25 and –0.7 electrons per unit cell, respectively) indicating the QI energy with a red dashed horizontal line. d) Local density of states at the Fermi level for (b) and outline of the construction of large-scale q-NPG devices by unit cell repetition along the *x* and *y* periodic directions. e,f) Bond current maps of injected currents in large-scale devices (268 800 atoms) upon gating -7.1×10^{12} e cm^{-2} and -2.0×10^{13} e cm^{-2}, respectively. Small red dots at the lower region of the devices indicate the point of current injection. Regions with high current density are shown in bright yellow and those with low or no current density are shown in dark purple, as indicated with color bars.

of electronic coupling between neighboring GNR channels[41] (see κ_c in Figure 3c) due to QI taking place within the quinoidal bridges at these gate fillings.

2.3. n-type Gating – Spin Filtering

To study the effect of n-doping we simulate a positively charged plane which induces an electron accumulation in q-NPG. Contrary to p-doping, electron doping fills in the previously empty quinoidal flat bands (see Figure 2c,d) which, interestingly, leads to an increasing net spin population with increasing gate, as shown in **Figure 4**a. Such spin polarization does not appear in the analogous aryl-connected NPG under the same applied gates (see Figure S4, Supporting Information) and so this effect may be exclusively associated to the quinoidal functionality. Indeed, taking a look at the atomically-resolved spin population map shown in Figure 4b, we see that spin is strongly localized in the quinone bridges, and particularly on the oxygen atoms generating the quinoidal configuration. This spin polarization is consistent with the partial reduction (i.e., electron addition) of the quinoidal aryl rings which, as schematically represented in Figure 4c, acquire an open-shell (i.e., radical) character. This result is in agreement with other studies which have reported spin polarization (open-shell character) of quinoidal derivatives by means of N-doping,[47–49] electrochemical reduction,[50] and surface chemisorption.[51] The magnetic coupling between the spin-polarized quinone units is rather weak both along the *x* and *y* directions, as shown with the nearly energetic degeneracy between the ferromagnetic solution with other antiferromagnetic spin configurations (see Figure S5, Supporting Information). This is typical for paramagnetic ground states, however, in such situations, the application of moderate magnetic fields, as regularly done for graphene,[52] may easily

© 2021 The Authors. Advanced Functional Materials published by Wiley-VCH GmbH

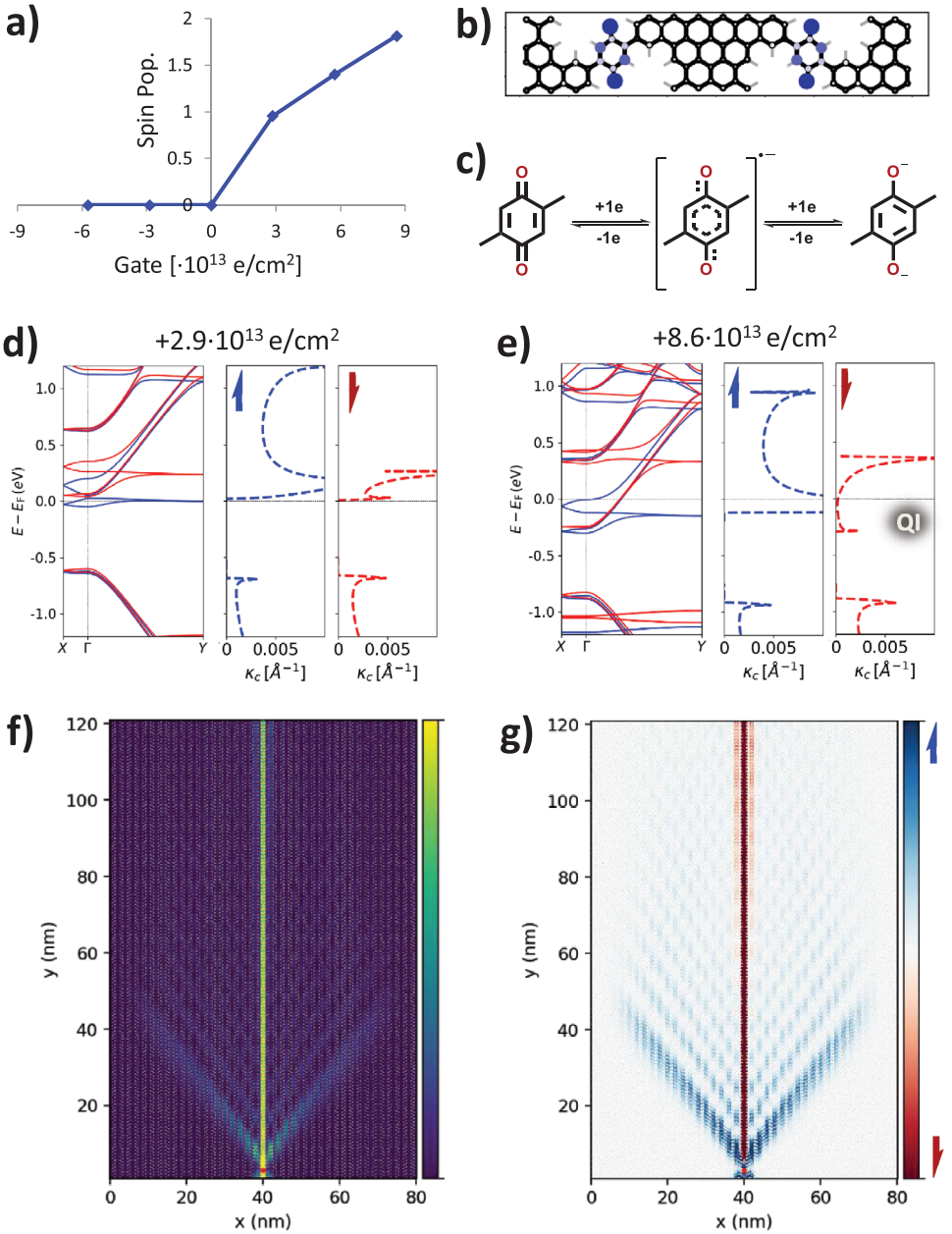

Figure 4. a) Total spin population in the q-NPG unit cell for various p-type and n-type gates. b) Atomically-resolved spin population map for the $+8.6 \times 10^{13}$ e cm^{-2} gated case. c) Chemical sketches of different redox states for p-benzoquinone. Spin-resolved (spin up: blue; spin down: red) band structures (left panels) and κ_c spectra (right panels) for d) $+2.9 \times 10^{13}$ e cm^{-2} and e) $+8.6 \times 10^{13}$ e cm^{-2} gates (+1 and +3 electrons per unit cell, respectively). f) Bond current maps for the $+8.6 \times 10^{13}$ e cm^{-2} gate. Regions with high current density are shown in bright yellow and those with low or no current density are shown in dark purple, as indicated with color bars. g) Associated net spin polarization map of bond currents (spin-up: blue; spin-down: red). Small red dots at the lower region of the devices indicate the point of injection (f,g).

populate the ferromagnetic state of the material (Figure 4b), which is the most promising one for spintronic applications. Focusing thus on the ferromagnetic solution, Figure 4d,e shows the band structure and κ_c spectra for $+2.9 \times 10^{13}$ e cm^{-2} and $+8.6 \times 10^{13}$ e cm^{-2} gates, respectively. There we may see that the previously empty flat quinoidal bands are filled only in the spin-up (blue) channel, creating a strong spin asymmetry in the resulting κ_c spectra (Figure 4d). With higher applied gates such spin-polarized bands become strongly hybridized with the GNR longitudinal bands (see Figure S6, Supporting Information), making it increasingly difficult to unambiguously distinguish between bridge quinoidal states and GNR states, because all bands acquire a strong longitudinal character.

As shown with the κ_c spectra in the right panel of Figure 4e, for relatively high electron dopings (e.g., $+8.6 \times 10^{13}$ e cm^{-2}) the electronic coupling between neighboring GNRs at the E_F is very high in the spin-up channel, but it is almost entirely depleted in the spin-down channel. This effect may be understood by

© 2021 The Authors. Advanced Functional Materials published by Wiley-VCH GmbH

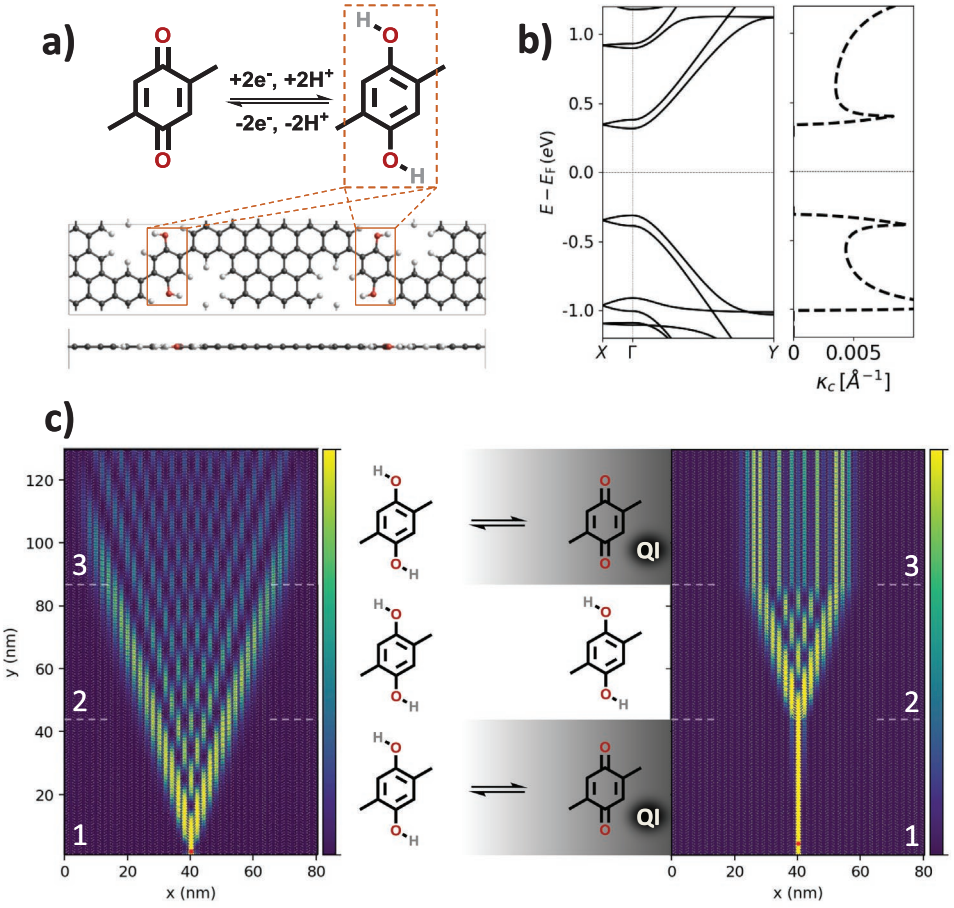

Figure 5. a) Chemical sketch of the electrochemical reduction of para-benzoquinone (top) and optimized periodic structure of the Hq-NPG (bottom) where the four oxygen atoms of q-NPG have been passivated with hydrogen atoms. b) Electronic band structure for the Hq-NPG and associated κ_c spectra. c) Bond current maps for injected currents in the occupied states ($E - E_F = -0.75$ eV) of the Hq-NPG (left) and a hybrid Hq-NPG/q-NPG (right) where regions 1 and 3 (see horizontal dashed white lines) have been de-hydrogenated as represented in the middle panel. Small red dots at the lower area of the devices indicate the point of injection. Regions with high current density are shown in bright yellow and those with low or no current density are shown in dark purple, as indicated with color bars.

the fact that only the spin-up quinoidal bands are filled, and so "open", whereas the spin-down quinoidal states remain empty, and so "closed" due to QI (Figure 4e).[39] This happens approximately in the gate window between $+5.7 \times 10^{13}$ and $+8.6 \times 10^{13}$ e cm^{-2} (see Figure S7, Supporting Information). In order to study the potentially appealing spintronic effects of such state, we constructed large-scale gated q-NPG devices based on a parameterized spin-polarized TB model (see DFT benchmark in Figure S8, Supporting Information). Figure 4f shows the bond currents map for the $+8.6 \times 10^{13}$ e cm^{-2} gated q-NPG, where we may see that part of the currents are being significantly spread forming the Talbot interference pattern,[37] whereas another fraction of them are strongly confined in the single GNR where they were injected. By plotting the corresponding spin-polarization of currents in Figure 4f (see Section 4) we may see that spreading electrons are mostly spin-up, whereas the fully confined currents are entirely spin-down polarized. Such an appealing spin-filtering effect arises from the electronic "opening" of the quinone bridges in the spin-up channel, while maintaining the QI blockade for spin-down currents.

2.4. Electrochemistry: Top-Down Engineering

Finally, inspired by single-molecule break junction transport measurements,[43] we consider the electrochemical reduction of the quinone oxygen groups with hydrogen atoms as a tool to restore, in a permanent fashion, the aromatic character of bridges (see **Figure 5**a) and so the electronic communication between GNRs. Figure 5a,b shows the optimized atomic structure of the fully passivated material, the para-hydroquinone-NPG (Hq-NPG), and its associated band structure, respectively. Similarly as for the q-NPG, we focus on the fully planar geometry, without loss of electronic information (see Figure S9, Supporting Information), which allows for large-scale device modelling. As shown in Figure 5b, hydrogenation restores the electron–hole symmetric band structure which is qualitatively similar to that of the fabricated NPG.[35] Thus the most significant changes compared to the parent q-NPG are the absence of the unoccupied quinoidal flat band close to the E_F and the disappearance of QI at the valence band. As a result, the electronic coupling between GNR channels is restored for the occupied

© 2021 The Authors. Advanced Functional Materials published by Wiley-VCH GmbH

states (see κ_c spectra in the right panel in Figure 5b) and, consequently, upon applying positive gates injected currents fully spread throughout the 2D material (see Figure S10, Supporting Information) as opposed to the q-NPG where full confinement occurs at those same gates (Figure 3f).

The ability to activate/deactivate QI in the occupied states by hydrogenation/de-hydrogenation appears as an appealing post-processing tool to top-down engineer the spatial distribution of currents in NPGs. It has been recently shown that it is possible to remove hydrogen atoms from the edge of carbon nanostructures with atomic precision by applying voltage pulses with a STM tip.[12,13,33] Other experiments have also shown that on-surface formation of carbon nanostructures may be enhanced[53] or tuned[54] upon exposure to atomic hydrogen. Inspired by these experiments we study the effect on quantum transport of a regional dehydrogenation of a previously fabricated Hq-NPG sample. For that we construct a nearest neighbor tight binding (TB) model capturing the electronic structure of the q-NPG and Hq-NPG, respectively (see DFT benchmark in Figures S11 and S12, Supporting Information and Section 4 for details) which allows modeling large-scale carbon heterostructured devices.[41] Left panel in Figure 5c shows the spreading of injected currents in the occupied bands ($E - E_F = -0.75$ eV) of a Hq-NPG large-scale device, in agreement with the associated interchannel electronic coupling (see κ_c spectra; right panel in Figure 5b). Hydrogen removal in the bottom and top regions of the device (1 and 3 in left panel of Figure 5c) which, in principle, could be done with atomic precision,[12,13,33] restores QI in those areas,[43] as schematically represented in the middle panel in Figure 5c. The spatial distribution of injected currents at the same energy ($E - E_F = -0.75$ eV) in the resulting hybrid Hq-NPG/q-NPG device is shown in the right panel of Figure 5c. As we may see, injected currents at the bottom region (1) remain fully confined, due to QI, until they reach the hydrogenated area of the device (2), at $\approx y = 44$nm, where the interchannel electronic communication is restored and, consequently, currents spread through a number of GNRs. Once the currents hit the top dehydrogenated region of the device (3), at $y = 88$ nm, interchannel decoupling due to QI occurs again, thus freezing the spreading pattern generated in region 2 up to the end of the device. By then passivating with atomic hydrogen larger areas of the device (i.e., increasing the size of region 2) one can achieve nanometric control over current confinement in region 3 (see Figure S13, Supporting Information). We note that such process should be reversible, and so exposure to atomic hydrogen[53,54] of regions 1 and 3 should recover the fully electronically coupled device shown in the left panel of Figure 5c (Hq-NPG). On the other hand, further hydrogen removal in region 2 in the hybrid device leads to a fully decoupled array of GNRs (q-NPG) and hence completely confines injected currents (Figure 3f).

3. Conclusion

In this work we study, via first principles DFT calculations and large-scale transport simulations, the use of electroactive molecules as bridges between GNRs in NPGs, as a tool to externally control the spatial distribution of injected currents in the 2D carbon nanomaterials. As recently shown in single-molecule break-junction experiments, quinones have an electrochemically dependent QI, and so tunable conductance.[43] Inspired by such experiments, we design the new q-NPG, where GNRs are bridged by para-benzoquinone. Analysis of the resulting electronic structure demonstrates that GNRs are electronically coupled for the unoccupied states, but electronically decoupled for the occupied ones. In order to assess the technological potential of this electron/hole asymmetry we model the application of electrostatic gates to large-scale q-NPG devices, and simulate the local injection of currents. We find that upon hole doping q-NPG, injected currents remain fully confined in the single GNR where they were injected for distances longer than 100 nm, due to QI.[41] On the other hand, electron doping erases QI at the quinone bridges, but only for one spin channel, which gives rise to appealing spin filtering effects, whereby spin-up currents spread through the entire 2D material whereas spin-down currents become fully confined in a single GNR channel.

Finally, we also test the effect of electrochemical reduction[43] via hydrogen passivation of oxygen atoms in the quinoidal bridges. Our results demonstrate that such chemical process permanently restores GNRs electronic coupling for both occupied and unoccupied states within the resulting Hq-NPG. Recent experiments have shown that it is possible to remove hydrogen atoms at the edges of graphene nanostructures with atomic precision by application of voltage pulses with an STM tip.[12,13,33] We demonstrate that atomically precise hydrogen removal could be used as a post-processing tool for Hq-NPG in order to restore QI for specific areas in the 2D material and, as a result, top-down engineer the spatial distribution of injected currents with nanometer precision.

Overall, our results demonstrate the potential of integrating electroactive molecules as bridges between GNRs in NPGs, to achieve electrochemically tunable quantum transport. GNRs have already been tested in solid-state devices,[23–26] however, in order to realize more complex functionality at the nanoscale it is required to fabricate more sophisticated nanostructures such as GNR heterostructures[30–34] or NPGs.[35,36] In this work we propose a simple and generally applicable recipe to externally control the spatial distribution of currents in such type of nanostructures, which represents a key step towards the long-term goal of carbon nanoelectronics. It is imperative to consider in the future the effect of other external variables such as finite temperatures or the interaction with substrates, but the experimental demonstration of QI-tuned electric conductance in quinone single-molecule experiments[43] supports the technological applicability of our proposal.

4. Experimental Section

All considered NPGs were modeled under the density functional theory (DFT) approach using the GGA-PBE[45] exchange-correlation functional, a single-ζ basis set with 0.02 Ry energy shift, norm-conserving Troullier–Martins pseudopotentials, a real-space mesh cutoff of 400 Ry, and a $15 \times 51 \times 1$ Monkhorst–Pack k-point mesh, as implemented in the SIESTA software.[55,56] The unit cells, orthogonal, and periodic, were fully optimized, including the cell parameters, until all forces were below 0.04 eV Å^{-1}. LDA (LSD) and hybrid DFT type functionals (CA[57,58] and HSE06,[46] respectively) provide qualitatively similar results, showing only minor quantitative differences from PBE, such as a slightly larger band splitting at the onset of the valence band for LDA (see Figure S1, Supporting Information). The authors note HSE06

© 2021 The Authors. Advanced Functional Materials published by Wiley-VCH GmbH

calculations (using a screening omega parameter[59] of 0.11 Bohr^{-1}) were run with the all-electron FHI-AIMS software,[60,61] using Tier-1 light numerical atom-centered orbital (NAO) basis set[62] and the same optimization setup as the Siesta calculations. The external application of electrostatic gates was modeled by fixing charges on a plane parallel to the 2D materials at 15 Å distance.[63] For each applied gate we have fully optimized the materials' atomic structure and cell parameters to capture any relaxation mechanism arising from the addition or subtraction of charge. Small out-of-plane twisting of the quinone bridges may occur for some of the considered materials (e.g., Hq-NPG) however, as shown in the Supporting Information, the resulting electronic band structures were qualitatively the same as for the fully planar structures. Therefore, all 2D materials were considered in their planar conformation in order to facilitate the transport simulations in large-scale devices.

Large-scale quantum transport was modeled by extracting the on-site and coupling elements associated to carbon and oxygen p_z orbitals from the DFT Hamiltonian to parameterize a more computationally efficient tight-binding (TB) model which properly captured the low-energy spectra. This procedure, carried out using the open-source Python-based SISL utility,[64] allowed to retain the full interaction range of the DFT basis set, and the self-consistent effects of electrostatic gates and hydrogen passivation on the electronic structure of NPGs. Only the more involved hybrid Hq-NPG/q-NPG structures, considered in the last section, were modeled by using an orthogonal nearest neighbor TB parameterization with hopping $t_{ij} = -2.7$ eV for all C and O atoms in the NPG geometries. In particular, for q-NPG the on-site energies were set to $\varepsilon_i = 0.2$ and -1.1 eV for C and O sites, respectively. Instead, for Hq-NPG we use $\varepsilon_i = 0$ eV for C sites and model the effect of hydrogenation by using $\varepsilon_i = -4$ eV at the O sites. All TB hamiltonians were benchmarked against the original DFT band structures (see Supporting Information). Large scale device TB models were constructed by repeating the respective NPG unit cells 20× along the *x*-direction and 140× along the *y*-direction, corresponding to NPG samples composed of ≈268 800 atoms. Such large structures were then fed to the open-source TBtrans code[56] to simulate quantum (spin-polarized) transport in the devices using the Green's function formalism.[65–67] Current injection was simulated via a constant, on-site broadening $i\Gamma$ self-energy in the device Green's function[68] localized on a single atom at the bottom of the central GNR in the NPG sample. The value of Γ, acting mainly as a scaling factor for injected currents, was set to 1 eV. This approach allowed to simulate in a simple, but effective, manner the current injection by a probe microscopy tip in chemical contact with one atom.[37] Currents were drained into two NPG-like electrodes semi-infinite toward *y* and $-y$ directions, and absorbed by 20 nm wide regions at the left and right sides of the device equipped with complex absorbing potentials (CAP),[69,70] thus avoiding electronic back-reflection at the nonperiodic walls of the device. The spatial current flow was analyzed by plotting 2D bond-current maps, summing up all spin-up and spin-down positive-valued bond-currents flowing out of each atom, scaling the color-map in proportion to the current magnitude, so that areas with low to zero current are dark. The net spin-polarization of currents was analyzed by plotting the normalized difference between vector current maps for spin-up and spin-down, using a symmetric color-map where white indicates zero net spin polarization of currents, or no currents, and the white-blue (white-red) color-range is associated to spin-up (spin-down) polarized currents. All maps were generated using SISL.[64]

Supporting Information

Supporting Information is available from the Wiley Online Library or from the author.

Acknowledgements

The authors acknowledge useful conversations with Dr Aran Garcia-Lekue. Financial support by the Danmarks Frie Forskningsfond (4184-00030) and Villum Fonden (00013340) is gratefully acknowledged. The Center for Nanostructured Graphene (CNG) is sponsored by the Danish National Research Foundation (DNRF103). I.A. is grateful for support from the Alexander von Humboldt Foundation. Computer facilities of the Freie Universität Berlin (ZEDAT) are acknowledged for computer time.

Open access funding enabled and organized by Projekt DEAL.

Conflict of Interest

The authors declare no conflict of interest.

Data Availability Statement

The data that support the findings of this study are available from the corresponding author upon reasonable request.

Keywords

density functional theory, electrochemical, engineering, graphene nanoribbons, nanoporous graphene, quantum transport, spin filtering

Received: April 28, 2021
Revised: June 18, 2021
Published online: July 19, 2021

[1] L. Grill, M. Dyer, L. Lafferentz, M. Persson, M. V. Peters, S. Hecht, *Nat. Nanotechnol.* **2007**, *2*, 687.
[2] X. H. Liu, C. Z. Guan, D. Wang, L. J. Wan, *Adv. Mater.* **2014**, *26*, 6912.
[3] Q. Fan, J. M. Gottfried, J. Zhu, *Acc. Chem. Res.* **2015**, *48*, 2484.
[4] G. Galeotti, F. De Marchi, E. Hamzehpoor, O. MacLean, M. Rajeswara Rao, Y. Chen, L. V. Besteiro, D. Dettmann, L. Ferrari, F. Frezza, P. M. Sheverdyaeva, R. Liu, A. K. Kundu, P. Moras, M. Ebrahimi, M. C. Gallagher, F. Rosei, D. F. Perepichka, G. Contini, *Nat. Mater.* **2020**, *19*, 874.
[5] M. Bieri, M. Treier, J. Cai, K. Aït-Mansour, P. Ruffieux, O. Gröning, P. Gröning, M. Kastler, R. Rieger, X. Feng, K. Müllen, R. Fasel, *Chem. Commun.* **2009**, *2009*, 6919.
[6] C. Steiner, J. Gebhardt, M. Ammon, Z. Yang, A. Heidenreich, N. Hammer, A. Görling, M. Kivala, S. Maier, *Nat. Commun.* **2017**, *8*, 14765.
[7] B. Yuan, C. Li, Y. Zhao, O. Gröning, X. Zhou, P. Zhang, D. Guan, D. Guan, Y. Li, Y. Li, H. Zheng, H. Zheng, C. Liu, C. Liu, Y. Mai, P. Liu, W. Ji, J. Jia, J. Jia, S. Wang, S. Wang, *J. Am. Chem. Soc.* **2020**, *142*, 10034.
[8] M. Di Giovannantonio, Q. Chen, J. I. Urgel, P. Ruffieux, C. A. Pignedoli, K. Müllen, A. Narita, R. Fasel, *J. Am. Chem. Soc.* **2020**, *142*, 12925.
[9] C.-H. Shu, M.-X. Liu, Z.-Q. Zha, J.-L. Pan, S.-Z. Zhang, Y.-L. Xie, J.-L. Chen, D.-W. Yuan, X.-H. Qiu, P.-N. Liu, *Nat. Commun.* **2018**, *9*, 2322.
[10] K. Biswas, J. I. Urgel, A. Sánchez-Grande, S. Edalatmanesh, J. Santos, B. Cirera, P. Mutombo, K. Lauwaet, R. Miranda, P. Jelínek, N. Martín, D. Écija, *Chem. Commun.* **2020**, *56*, 15309.
[11] B. Cirera, A. Sánchez-Grande, B. de la Torre, J. Santos, S. Edalatmanesh, E. Rodríguez-Sánchez, K. Lauwaet, B. Mallada, R. Zbořil, R. Miranda, O. Gröning, P. Jelínek, N. Martín, D. Ecija, *Nat. Nanotechnol.* **2020**, *15*, 437.
[12] S. Mishra, D. Beyer, K. Eimre, S. Kezilebieke, R. Berger, O. Gröning, C. A. Pignedoli, K. Müllen, P. Liljeroth, P. Ruffieux, X. Feng, R. Fasel, *Nat. Nanotechnol.* **2020**, *15*, 22.

© 2021 The Authors. Advanced Functional Materials published by Wiley-VCH GmbH

[13] J. Li, S. Sanz, J. Castro-Esteban, M. Vilas-Varela, N. Friedrich, T. Frederiksen, D. Peña, J. I. Pascual, *Phys. Rev. Lett.* **2020**, *124*, 177201.
[14] Q. Fan, D. Martin-Jimenez, S. Werner, D. Ebeling, T. Koehler, T. Vollgraff, J. Sundermeyer, W. Hieringer, A. Schirmeisen, J. M. Gottfried, *J. Am. Chem. Soc.* **2020**, *142*, 894.
[15] A. Narita, X.-Y. Wang, X. Feng, K. Müllen, *Chem. Soc. Rev.* **2015**, *44*, 6616.
[16] K. Nakada, M. Fujita, G. Dresselhaus, M. S. Dresselhaus, *Phys. Rev. B* **1996**, *54*, 17954.
[17] Y.-W. Son, M. L. Cohen, S. G. Louie, *Nature* **2006**, *444*, 347.
[18] J. Cai, P. Ruffieux, R. Jaafar, M. Bieri, T. Braun, S. Blankenburg, M. Muoth, A. P. Seitsonen, M. Saleh, X. Feng, K. Müllen, R. Fasel, *Nature* **2010**, *466*, 470.
[19] Z. Chen, A. Narita, K. Müllen, *Adv. Mater.* **2020**, *32*, 2001893.
[20] Y. Yano, N. Mitoma, H. Ito, K. Itami, *J. Org. Chem.* **2020**, *85*, 4.
[21] V. Saraswat, R. M. Jacobberger, M. S. Arnold, *ACS Nano* **2021**, *15*, 3674.
[22] Z. Guan, C. Si, S. Hu, W. Duan, *Phys. Chem. Chem. Phys.* **2016**, *18*, 12350.
[23] A. N. Abbas, G. Liu, A. Narita, M. Orosco, X. Feng, K. Müllen, C. Zhou, *J. Am. Chem. Soc.* **2014**, *136*, 7555.
[24] J. P. Llinas, A. Fairbrother, G. Borin Barin, W. Shi, K. Lee, S. Wu, B. Y. Choi, R. Braganza, J. Lear, N. Kau, W. Choi, C. Chen, Z. Pedramrazi, T. Dumslaff, A. Narita, X. Feng, K. Müllen, F. Fischer, A. Zettl, P. Ruffieux, E. Yablonovitch, M. Crommie, R. Fasel, J. Bokor, *Nat. Commun.* **2017**, *8*, 633.
[25] N. Richter, Z. Chen, A. Tries, T. Prechtl, A. Narita, K. Müllen, K. Asadi, M. Bonn, M. Kläui, *Sci. Rep.* **2020**, *10*, 1988.
[26] M. El Abbassi, M. Perrin, G. B. Barin, S. Sangtarash, J. Overbeck, O. Braun, C. Lambert, Q. Sun, T. Prechtl, A. Narita, K. Mullen, P. Ruffieux, H. Sadeghi, R. Fasel, M. Calame, *ACS Nano* **2019**, *14*, 5754.
[27] N. Friedrich, P. Brandimarte, J. Li, S. Saito, S. Yamaguchi, I. Pozo, D. Penã, T. Frederiksen, A. Garcia-Lekue, D. Sánchez-Portal, J. I. Pascual, *Phys. Rev. Lett.* **2020**, *125*, 146801.
[28] M. C. Chong, N. Afshar-Imani, F. Scheurer, C. Cardoso, A. Ferretti, D. Prezzi, G. Schull, *Nano Lett.* **2018**, *18*, 175.
[29] P. H. Jacobse, A. Kimouche, T. Gebraad, M. M. Ervasti, J. M. Thijssen, P. Liljeroth, I. Swart, *Nat. Commun.* **2017**, *8*, 119.
[30] J. Cai, C. A. Pignedoli, L. Talirz, P. Ruffieux, H. Söde, L. Liang, V. Meunier, R. Berger, R. Li, X. Feng, K. Müllen, R. Fasel, *Nat. Nanotechnol.* **2014**, *9*, 896.
[31] C. Bronner, R. A. Durr, D. J. Rizzo, Y.-L. Lee, T. Marangoni, A. M. Kalayjian, H. Rodriguez, W. Zhao, S. G. Louie, F. R. Fischer, M. F. Crommie, *ACS Nano* **2018**, *12*, 2193.
[32] O. Gröning, S. Wang, X. Yao, C. A. Pignedoli, G. Borin Barin, C. Daniels, A. Cupo, V. Meunier, X. Feng, A. Narita, K. Müllen, P. Ruffieux, R. Fasel, *Nature* **2018**, *560*, 209.
[33] J. Li, S. Sanz, M. Corso, D. J. Choi, D. Peña, T. Frederiksen, J. I. Pascual, *Nat. Commun.* **2019**, *10*, 200.
[34] J. Li, N. Friedrich, N. Merino, D. G. de Oteyza, D. Peña, D. Jacob, J. I. Pascual, *Nano Lett.* **2019**, *19*, 3288.
[35] C. Moreno, M. Vilas-Varela, B. Kretz, A. Garcia-Lekue, M. V. Costache, M. Paradinas, M. Panighel, G. Ceballos, S. O. Valenzuela, D. Peña, A. Mugarza, *Science* **2018**, *360*, 199.
[36] P. H. Jacobse, R. D. McCurdy, J. Jiang, D. J. Rizzo, G. Veber, P. Butler, R. Zuzak, S. G. Louie, F. R. Fischer, M. F. Crommie, *J. Am. Chem. Soc.* **2020**, *142*, 13507.
[37] G. Calogero, N. R. Papior, B. Kretz, A. Garcia-Lekue, T. Frederiksen, M. Brandbyge, *Nano Lett.* **2018**, *19*, 576.
[38] M. Shekhirev, P. Zahl, A. Sinitskii, *ACS Nano* **2018**, *12*, 8662.
[39] Y. Tsuji, R. Hoffmann, M. Strange, G. C. Solomon, *Proc. Natl. Acad. Sci. USA* **2016**, *11*, E413.
[40] C. R. Arroyo, S. Tarkuc, R. Frisenda, J. S. Seldenthuis, C. H. M. Woerde, R. Eelkema, F. C. Grozema, H. S. J. van der Zant, *Angew. Chem., Int. Ed.* **2013**, *52*, 3152.
[41] G. Calogero, I. Alcón, N. Papior, A.-P. Jauho, M. Brandbyge, *J. Am. Chem. Soc.* **2019**, *141*, 13081.
[42] T. Markussen, R. Stadler, K. S. Thygesen, *Nano Lett.* **2010**, *10*, 4260.
[43] N. Darwish, I. Díez-Pérez, P. Da Silva, N. Tao, J. J. Gooding, M. N. Paddon-Row, *Angew. Chem., Int. Ed.* **2012**, *51*, 3203.
[44] A. Keerthi, B. Radha, D. Rizzo, H. Lu, V. Diez Cabanes, I. C. Y. Hou, D. Beljonne, J. Cornil, C. Casiraghi, M. Baumgarten, K. Müllen, A. Narita, *J. Am. Chem. Soc.* **2017**, *139*, 16454.
[45] J. P. Perdew, K. Burke, M. Ernzerhof, *Phys. Rev. Lett.* **1996**, *77*, 3865.
[46] J. Heyd, G. E. Scuseria, M. Ernzerhof, *J. Chem. Phys.* **2003**, *118*, 8207.
[47] M. Kaupp, M. Renz, M. Parthey, M. Stolte, F. Würthner, C. Lambert, *Phys. Chem. Chem. Phys.* **2011**, *13*, 16973.
[48] A. Heckmann, C. Lambert, *J. Am. Chem. Soc.* **2007**, *129*, 5515.
[49] L. K. Montgomery, J. C. Huffman, E. A. Jurczak, M. P. Grendze, *J. Am. Chem. Soc.* **1986**, *108*, 6004.
[50] P. M. Burrezo, N.-T. Lin, K. Nakabayashi, S. Ohkoshi, E. M. Calzado, P. G. Boj, M. A. Díaz García, C. Franco, C. Rovira, J. Veciana, M. Moos, C. Lambert, J. T. López Navarrete, H. Tsuji, E. Nakamura, J. Casado, *Angew. Chem., Int. Ed.* **2017**, *56*, 2898.
[51] M. R. Ajayakumar, C. Moreno, I. Alcón, F. Illas, C. Rovira, J. Veciana, S. T. Bromley, A. Mugarza, M. Mas-Torrent, *J. Phys. Chem. Lett.* **2020**, *11*, 3897.
[52] B. S. Jessen, L. Gammelgaard, M. R. Thomsen, D. M. A. Mackenzie, J. D. Thomsen, J. M. Caridad, E. Duegaard, K. Watanabe, T. Taniguchi, T. J. Booth, T. G. Pedersen, A. P. Jauho, P. Bøggild, *Nat. Nanotechnol.* **2019**, *14*, 340.
[53] C. Sánchez-Sánchez, J. I. Martínez, N. Ruiz del Arbol, P. Ruffieux, R. Fasel, M. F. López, P. L. de Andres, J. Á. Martín-Gago, *J. Am. Chem. Soc.* **2019**, *141*, 3550.
[54] R. Zuzak, A. Jančařík, A. Gourdon, M. Szymonski, S. Godlewski, *ACS Nano* **2020**, *14*, 13316.
[55] J. M. Soler, E. Artacho, J. D. Gale, A. García, J. Junquera, P. Ordejón, D. Sánchez-Portal, *J. Phys. Condens. Matter* **2002**, *14*, 2745.
[56] N. Papior, N. Lorente, T. Frederiksen, A. García, M. Brandbyge, *Comput. Phys. Commun.* **2017**, *212*, 8.
[57] D. M. Ceperley, B. J. Alder, *Phys. Rev. Lett.* **1980**, *45*, 566.
[58] J. P. Perdew, A. Zunger, *Phys. Rev. B* **1981**, *23*, 5048.
[59] A. V. Krukau, O. A. Vydrov, A. F. Izmaylov, G. E. Scuseria, *J. Chem. Phys.* **2006**, *125*, 224106.
[60] V. Havu, V. Blum, P. Havu, M. Scheffler, *J. Comput. Phys.* **2009**, *228*, 8367.
[61] V. Blum, R. Gehrke, F. Hanke, P. Havu, V. Havu, X. Ren, K. Reuter, M. Scheffler, *Comp. Phys. Comm.* **2009**, *180*, 2175.
[62] I. Y. Zhang, X. Ren, P. Rinke, V. Blum, M. Scheffler, *New J. Phys.* **2013**, *15*, 123033.
[63] N. Papior, T. Gunst, D. Stradi, M. Brandbyge, *Phys. Chem. Chem. Phys.* **2015**, *18*, 1025.
[64] N. Papior, *sisl*, **2021**, v0.11.0, https://github.com/zerothi/sisl.
[65] M. Brandbyge, J.-L. Mozos, P. Ordejón, J. Taylor, K. Stokbro, *Phys. Rev. B* **2002**, *65*, 165401.
[66] S. Datta, *Superlattices Microstruct.* **2000**, *28*, 253.
[67] K. K. Saha, B. K. Nikolić, V. Meunier, W. Lu, J. Bernholc, *Phys. Rev. Lett.* **2010**, *105*, 236803.
[68] J. Aprojanz, S. R. Power, P. Bampoulis, S. Roche, A. P. Jauho, H. J. W. Zandvliet, A. A. Zakharov, C. Tegenkamp, *Nat. Commun.* **2018**, *9*, 4426.
[69] H. Xie, Y. Kwok, F. Jiang, X. Zheng, G. Chen, *J. Chem. Phys.* **2014**, *141*, 164122.
[70] G. Calogero, N. R. Papior, P. Bøggild, M. Brandbyge, *J. Phys. Condens. Matter* **2018**, *30*, 364001.

© 2021 The Authors. Advanced Functional Materials published by Wiley-VCH GmbH